# Effect of Zn coprecipitation on the structure of layered Mn oxides

Shiliang Zhao[1], Qian Wang[2], Jingying Sun[3], Olaf J. Borkiewicz[4], Rixiang Huang[1], Emily M. Saad[1], Benjamin Fields[1], Shuo Chen[3], Mengqiang Zhu[2], Yuanzhi Tang[1]*

[1] School of Earth and Atmospheric Sciences, Georgia Institute of Technology, Atlanta, GA

[2] Department of Ecosystem Science and Management, University of Wyoming, Laramie, WY 82071

[3] Department of Physics and Texas Center for Superconductivity, University of Houston, Houston, TX 77204

[4] Advanced Photon Source, Argonne National Laboratory, Argonne, IL 60439

*Corresponding author. Email: yuanzhi.tang@eas.gatech.edu; Phone: 404-894-3814

**Abstract**

Mn oxides ($MnO_x$) are a group of ubiquitous metal oxides in the environment and can significantly affect the biogeochemical cycles of metals, nutrients, and contaminants. Due to their negative surface charge across a wide range of environmental conditions, metal cations have strong affinities for $MnO_x$, and the presence of metal cations during or after the formation of $MnO_x$ might significantly affect their structure and properties. This study systematically investigates the effects of $Zn^{2+}$ presence during mineral formation (i.e. coprecipitation) on the structure of acid birnessite and δ-$MnO_2$, two synthetic analogs that are structurally similar to fresh biogenic $MnO_x$ but with different crystallinity. For both acid birnessite and δ-$MnO_2$, $Zn^{2+}$ existed as surface adsorbed species at vacancy sites, interrupted layer stacking along *c* axis, and caused reductions of the lateral particle size. $Zn^{2+}$ also reduced Mn(III) contents in δ-$MnO_2$ layers, leaving more vacancy sites (capped by adsorbed $Zn^{2+}$). The reduction of layer stacking was more obvious for acid birnessite, while the modification of layer structure was more significant for δ-$MnO_2$. These structural changes will likely lead to modified reactivities of $MnO_x$ in natural systems.

**Keywords:** Manganese oxide, Birnessite, Zinc, Coprecipitation, Structure

## 1. Introduction

Manganese (Mn) oxides ($MnO_x$) are a group of metal oxides that are ubiquitous in nearly all environmental settings, such as fresh waters, marine nodules, soils, and sediments (Bargar et al., 2009; Bodeï et al., 2007; Lanson et al., 2008). $MnO_x$ can form through the oxidation of Mn(II) and this process is much faster when catalyzed by mineral surfaces or microorganisms. Previous studies have shown that the initial biogenic $MnO_x$ phases produced by bacteria (Learman et al., 2011a; Learman et al., 2011b; Villalobos et al., 2006) and fungi (Bargar et al., 2005; Grangeon et al., 2010; Saratovsky et al., 2009) at circumneutral pH are typically highly disordered and nanocrystalline phases that are structurally similar to hexagonal phyllomanganates (e.g. acid birnessite and δ-$MnO_2$) (Tebo et al., 2004). Due to their high surface area, large amount of vacancy sites, and negative surface charge across a wide range of pH conditions, $MnO_x$ are highly reactive for the adsorption and redox transformation of metals (e.g. Pb, Ni, Cr) (Charlet and Manceau, 1992; Gadde and Laitinen, 1974; Kawashima et al., 1986; Li et al., 2015; Nico and Zasoski, 2000), metalloids (e.g. As, Se) (Chang et al., 2012; Manceau et al., 2007), and organic compounds (Kung and McBride, 1988; Stone and Morgan, 1984), and can exert significant influences on the biogeochemical cycles of many important elements. From the materials chemistry aspect of view, hexagonal phyllomanganates are also important layered octahedral molecular sieves (OMS). The design of OMS with specific composition, structure, and morphology is of great interest for environmental, chemical, and material science research, due to their wide applications as catalysts, battery electrodes, adsorbents, and semiconductors (Lee et al., 2007; Li et al., 2006; Poizot et al., 2000; Yin et al., 2011a).

Metal cations such as $Ni^{2+}$, $Co^{2+}$, $Cu^{2+}$, $Pb^{2+}$, and $Zn^{2+}$ can either adsorb onto and/or incorporate into the layer vacancies and edge sites of birnessite (Drits et al., 2002; Hinkle et al.,

2017; Lanson et al., 2002b; Manceau et al., 2002; Manceau et al., 1997; Peña et al., 2015; Peña et al., 2010; Silvester et al., 1997; Simanova et al., 2015; Villalobos et al., 2005). Adsorption of non-redox sensitive metals on $MnO_x$ was shown to have limited effects on $MnO_x$ layer structure (Power et al., 2005; Villalobos et al., 2014b) (except a recent study on $Zn^{2+}$ sorption (Grangeon et al., 2012), as discussed later). Although numerous studies have examined the sorption and/or incorporation of metal cations on pre-formed $MnO_x$ (i.e. sorption system), much remain unknown on the impact of metal cation presence during $MnO_x$ formation (i.e. coprecipitation system) on the oxide structure, reactivity, and transformation, despite the obvious relevance in complex environmental settings. Several recent studies demonstrated significant impacts of metal coprecipitation on the structural properties of $MnO_x$, such as Mn(II, III) contents, vacancy site density, crystallinity, thermal stability, and surface area (Kamimura et al., 2013; Yin et al., 2011a; Yin et al., 2015b; Yin et al., 2014; Yin et al., 2013; Yin et al., 2011b; Yin et al., 2015c; Yin et al., 2012). For biogenic phyllomanganates, the presence of $Ni^{2+}$ can enhance vacancy site formation while $Ca^{2+}$ and $Na^{+}$ were shown to stabilize layer Mn(III) (Zhu et al., 2010). For abiotic hexagonal birnessite, coprecipitation of Ni, Co, Fe, and V were found to modify the surface area, layer stacking, oxidation states, and coherent scattering domain size of $MnO_x$ (Yin et al., 2011a; Yin et al., 2015b; Yin et al., 2014; Yin et al., 2012). These influences were shown to be metal specific and dependent on the compatibility of foreign metal ions with the $MnO_x$ structure (e.g. size/charge similarities to the structural Mn(III)/(IV) ions, crystal field stability energy), which was previously suggested to be reflected in the ratio of incorporated metal vs. surface complexed metal (i.e. incorporation/(incorporation + complexation) (Yin et al., 2011a; Yin et al., 2015b; Yin et al., 2013; Yin et al., 2015c; Yin et al., 2012). The degree of compatibility and amount of metal ion incorporation was found to increase in the order of $Zn^{2+} < Cu^{2+} < Ni^{2+} < Co^{3+}$, with the metal

impact on structure modification in the reverse order (Yin et al., 2011a; Yin et al., 2013; Yin et al., 2012). These modified structural properties were shown to lead to differences in adsorptive capacities towards metal cations (e.g. $Pb^{2+}$, $Zn^{2+}$) (Li et al., 2015; Yin et al., 2015b; Yin et al., 2014; Yin et al., 2011b; Yin et al., 2012) and anions (e.g. arsenate) (Villalobos et al., 2014b), oxidative capability, as well as catalytic (Wang et al., 2016; Yin et al., 2015a) and electrochemical properties (Liu et al., 2015).

Among the transition metals (e.g. Co, Ni, Cu, Fe, Zn) that are commonly found to associate with $MnO_x$ in natural environments, Zn shows the least structural compatibility (Kwon et al., 2013; Yin et al., 2011a; Yin et al., 2013; Yin et al., 2012). $Zn^{2+}$ has not been found to incorporate into the layer vacancy sites of synthetic or biogenic birnessite, but instead predominantly adsorbs above/below the vacancy sites. Interestingly, the coordination environment of $Zn^{2+}$ on $MnO_x$ is dependent on $Zn^{2+}$ concentration as well as $MnO_x$ crystallinity (Grangeon et al., 2012). Tetrahedrally coordinated $Zn^{2+}$ ($Zn^{IV}$) at low $Zn^{2+}$ concentrations can change to octahedral coordination ($Zn^{VI}$) with increasing $Zn^{2+}$ loading (Manceau et al., 2002; Toner et al., 2006; Trivedi et al., 2001). A recent study showed that adsorbed $Zn^{2+}$ can reduce the amount of Mn(III) ions in δ-$MnO_2$ layers, leaving more vacancy sites (capped by adsorbed $Zn^{2+}$) (Grangeon et al., 2012). $Zn^{2+}$ adsorption can also cause the dissolution of birnessite and result in smaller coherent scattering domain size in the *a-b* plane as calculated by X-ray diffraction (XRD) fitting (Grangeon et al., 2012). Only two previous studies have examined the effect of $Zn^{2+}$ coprecipitation on $MnO_x$ structure, but no consensus was reached. Yu et al. found that the presence of $Zn^{2+}$ during the formation of fungal $MnO_x$ inhibited the crystal growth and modified the layer stacking of $MnO_x$ (Yu et al., 2013). Boonfueng et al. found that the presence of $Zn^{2+}$ during biogenic $MnO_x$ formation resulted in large $Zn^{2+}$ sequestration (likely due to surface sorption), but with no obvious changes

in $MnO_x$ local structure (Boonfueng et al., 2009). Given the low compatibilities of $Zn^{2+}$ with phyllomanganate structure, as well as its unique dependence of coordination environment on phyllomanganate crystallinity, a systematic study is highly desired to reveal the impact of this environmentally abundant element on the composition, surface properties, morphology, structural properties, as well as subsequent reactivity (e.g. sorptive, redox) of $MnO_x$.

This study examines the impact of $Zn^{2+}$ coprecipitation on the structural properties of two phyllomanganates with different structural order, acid birnessite and δ-$MnO_2$. $Zn^{2+}$ association with natural $MnO_x$ was found to be 0–0.5% (Zn/Mn molar ratio) in marine nodules (Childs, 1975; Jenkyns, 1970; Marcus et al., 2004) and soils (Manceau et al., 2003). This ratio can reach 3% in coal mine drainage treatment systems where Mn(II)-oxidizing microbes thrive (Tan et al., 2010), and can be as high as 46% in contaminated sediments (Lanson et al., 2008). This ratio can be even higher locally (Manceau et al., 2007). Since $Zn^{2+}$ sequestration is known to be affected by phyllomanganate structure and crystallinity, we compared acid birnessite and δ-$MnO_2$, two structurally similar phyllomanganate phases but with different structural order. Compared to δ-$MnO_2$, acid birnessite has better crystallinity, more layer stacking along *c* axis, larger layer dimension, and lower surface area (Manceau et al., 2013; Villalobos et al., 2003). Because $Zn^{VI}$ stabilization is weaker between incoherently stacked and laterally smaller layers (Kwon et al., 2009), its prevalence on δ-$MnO_2$ was shown to be two times lower than on acid birnessite at similar Zn/Mn loadings (Grangeon et al., 2012; Yu et al., 2013). Therefore, it is possible that $Zn^{2+}$ coprecipitation can have different effects on the structural properties of these two $MnO_x$ phases with different crystallinity.

Compared to previous studies on Zn sorption on pre-formed $MnO_x$ (Boonfueng et al., 2009; Drits et al., 2002; Grangeon et al., 2012; Lanson et al., 2002b; Manceau et al., 2002; Silvester et al., 1997; Toner et al., 2006), in this study Zn

was added during the formation of Mn oxides (i.e. Zn coprecipitation). Although Zn was also found to exist as surface adsorbed species in this coprecipitation system (details in results section), more significant effects were observed on $MnO_x$ structure compared to Zn sorption systems. By exploring two synthetic $MnO_x$ phases with similar structure but different structure order, our system eliminated the potential toxicity effects associated with biogenic $MnO_x$ systems, and allowed thorough investigation on the effect of $MnO_x$ structure order. We conducted systematic characterization of the Zn-coprecipitated $MnO_x$ phases, by combining a suite of complementary techniques that are capable of probing mineral surface properties, morphology, and structure orders at various ranges, including BET surface area analysis, zeta-potential measurements, Zn and Mn X-ray absorption spectroscopy (XAS), X-ray diffraction (XRD), pair distribution function (PDF) analysis of X-ray total scattering, and high resolution transmission electron microscopy (HRTEM). Information obtained from this study provides a better understanding of the impacts of $Zn^{2+}$ coprecipitation on the structural properties of two environmentally relevant $MnO_x$ phases, and points to the importance of considering metal coprecipitation effects for studies centered on $MnO_x$ reactivity in natural systems.

## 2. Methods

### 2.1. Synthesis of δ-$MnO_2$ and acid birnessite in the presence of $Zn^{2+}$

Both δ-$MnO_2$ and acid birnessite phases were synthesized in the absence or presence of a range of $Zn^{2+}$ concentrations. δ-$MnO_2$ synthesis followed a previous procedure (Zhu et al., 2012) where 160 mL $MnSO_4$ solution (0.30 mol $L^{-1}$) was pumped into a mixture of 160 mL $KMnO_4$ (5.0 g) and 180 mL NaOH (3.5 g) solutions at a speed of 25 mL $min^{-1}$ under vigorous stirring. Calculated amounts of $ZnSO_4$ was dissolved in the $MnSO_4$ solution to achieve Zn:total Mn molar

ratio of 0–20%. For acid birnessite synthesis, $ZnSO_4$ was dissolved in 45 mL of 6 mol $L^{-1}$ HCl solution to achieve Zn/total Mn molar ratio of 0–20%. This solution was then pumped at 1 mL $min^{-1}$ into 300 mL of boiling 0.667 mol $L^{-1}$ $KMnO_4$ solution under vigorous stirring (Villalobos et al., 2003). Previous studies on Mn oxide formation in the presence of $Zn^{2+}$ used Zn/Mn ratios of ~1–22% (Yu et al., 2013). After synthesis, the suspensions were cooled down (for birnessite) and the solid precipitates vacuum filtered (0.2 μm), rinsed with deionized (DI) water, dialyzed, and freeze-dried. Samples were labeled according to the starting Zn/Mn molar ratio and are referred to as pure or Zn-coprecipitated samples (see Table 1 for details). A portion of the dried solids was digested by aqua regia and analyzed for elemental composition using inductively coupled plasms – mass spectrometry (ICP-MS). Samples were also characterized for their morphology, surface, and structure properties using BET surface area analysis, zeta potential analysis, HRTEM, XRD, PDF, and XAS, as detailed below and in Supporting Information (SI) Text S1-S5.

### 2.2. X-ray absorption spectroscopy analysis

Mn and Zn K-edge XAS data were collected on both pure and Zn-coprecipitated birnessite and δ-$MnO_2$ samples to investigate their structural characteristics. Suspensions containing $MnO_x$ were vacuum filtered through 0.2 μm polycarbonate membranes and rinsed with DI water. The moist filter membranes loaded with $MnO_x$ wet pastes were mounted in an acrylic sample holder covered with Kapton tape. Samples were stored at -20 °C and thawed prior to analysis. XAS data were collected at Beamline 4-1 of the Stanford Synchrotron Radiation Lightsource (SSRL; Menlo Park, CA) using Si(220) monochromator and Beamlines 5-BM-D and 12-BM-B at the Advanced Photon Source (APS; Argonne National Laboratory, Lemont, IL) using Si(111) monochromators, all with 40% detuning to avoid higher order harmonics. Energy calibration used Mn or Zn foil.

XAS data were collected in both transmission and fluorescence mode using a Lytle detector (Beamlines 4-1 at SSRL and 12-BM-B at APS) or a vortex detector (Beamline 5-BM-D at APS). Both XANES (X-ray absorption near edge structure) and EXAFS (extended X-ray absorption fine structure) data were collected. Two to six scans were collected and averaged. Analysis of the Mn XANES spectra for each sample showed no photo-reduction of $MnO_x$ under the X-ray beam.

XAS data analysis was performed using the programs SIXPACK (Webb, 2005), Ifeffit (Ravel and Newville, 2005), and WINXAS (Ressler, 1998). Shell by shell fitting was conducted for both Mn and Zn EXAFS spectra to elucidate local coordination structures. Linear combination fitting (LCF) of the Mn XANES region was conducted to determine the relative percentage of Mn(II), Mn(III), and Mn(IV) species and the average oxidation state (AOS) following the method described in Manceau et al (Manceau et al., 2012). Manceau et al.(Manceau et al., 2012) compared the LCF results of Mn K-edge XANES with different reference sets and pointed out that reference sets with different structures might result in errors when determining AOS. Therefore, two reference compound sets with different Mn(II)/(III)/(IV) compounds were tested. The first set included $MnSO_4$(aq), $MnPO_4$ (ramsdellite), and K-birnessite, and the second set included $MnSO_4$(s), $Mn_2O_3$, and pyrolusite ($MnO_2$).

### 2.3. Pair distribution function (PDF) analysis of X-ray total scattering

Synchrotron high-energy X-ray total scattering data of the synthesized $MnO_x$ samples were collected at beamline 11-ID-B (~58.6 keV, $\lambda$ = 0.2117 Å) of the Advanced Photon Source (APS), Argonne National Laboratory, IL. Conversion of data from 2D to 1D was performed using the program Fit2D (Hammersley, 1998; Hammersley et al., 1996). The experimental total scattering structure function *S(Q)*, reduced experimental structure function *f(Q)*, and PDF, or *G(r)*, were

obtained using PDFgetX2 (Qiu et al., 2004). The PDFs were calculated from the Fourier transforms of these data truncated at 26 $Å^{-1}$.

## 3. Results

### 3.1. Chemical compositions

Composition analysis of the Zn-coprecipitated $MnO_x$ showed significant amount of $Zn^{2+}$ sequestration by the oxides (Table 1). Zn/Mn molar ratio in the final solids increased with increasing values of initial Zn/Mn ratio. However, under 20% Zn/Mn starting condition, acid birnessite was only able to sequester ~16% Zn/Mn, as compared to ~21% for δ-$MnO_2$. This higher $Zn^{2+}$ uptake capacity of δ-$MnO_2$ might be due to its intrinsic structural properties, as discussed later.

The presence of $Zn^{2+}$ significantly decreased the interlayer cation ($K^+$) content for birnessite, but has little impact on the content of interlayer cations ($K^+$ and $Na^+$) of δ-$MnO_2$ (Table 1). Total Mn content was similar for birnessite or δ-$MnO_2$ samples with different $Zn^{2+}$ loadings, except for a slight decrease at 20% Zn/Mn loading for acid birnessite. This suggests that $Zn^{2+}$ might have preferably replaced the interlayer cations in acid birnessite instead of substituting for Mn(III, IV) ions within the $MnO_6$ layers. This is consistent with previous studies where no $Zn^{2+}$ substitution into the layer structure was observed when $Zn^{2+}$ was sorbed on Mn oxides or was present during biogenic Mn oxide formation (Manceau et al., 2002; Toner et al., 2006; Yu et al., 2013).

### 3.2. Morphology of Mn oxides as revealed by HRTEM

HRTEM images revealed significant morphological modifications of Zn-coprecipitated

birnessite and δ-$MnO_2$ phases, as compared to their pure phases (Figure 1 and S1). In general, birnessite samples contain larger particles with multiple layer stacking, while δ-$MnO_2$ samples show much limited layer stacking and smaller lateral particle size. All phases aggregate heavily with curling features, and the aggregation was enhanced by Zn-coprecipitation, consistent with BET surface area measurements showing decreased surface area with increasing Zn/Mn ratio (Table 1). All δ-$MnO_2$ samples showed more intense curling morphology compared to acid birnessite samples.

In general, Zn-coprecipitation caused less layer stacking and smaller lateral layer size. The average number of stacking layers (along *c* axis) for each sample is summarized in Table 1. Pure δ-$MnO_2$ sample contained 5±1 layers and acid birnessite 11±3 layers. With increasing Zn/Mn ratio, the number of stacking layers decreased significantly from 11±3 to 5±1 for acid birnessite and from 5±1 to 4±1 for δ-$MnO_2$. It was difficult to quantitatively measure the lateral particle size from HRTEM images due to strong aggregation, but a general decrease in lateral particle size in the presence of $Zn^{2+}$ was observed in all acid birnessite and δ-$MnO_2$ samples (Figure 1 and S1).

### 3.3. Surface properties

BET specific surface area (SSA) is a commonly used parameter for evaluating Mn oxide adsorption and oxidation capabilities. In this study, the SSAs of pure acid birnessite and δ-$MnO_2$ were 27.4 and 221.9 $m^2/g$, respectively (Table 1), consistent with previously reported values of 19–40.5 $m^2/g$ for acid birnessite and 114–274 $m^2/g$ for δ-$MnO_2$ (Power et al., 2005; Villalobos et al., 2014b; Wang et al., 2016; Yin et al., 2013). For acid birnessite, with increasing Zn/Mn ratio, SSA first increased from 27.4 (p-bir) to 32.5 (5Zn-bir), then decreased to 19.3 $m^2/g$ (20Zn-bir). SSA can be affected by many factors including crystallite size and aggregation. Reduction in both

layer stacking and lateral layer size decreases crystallite size and increases surface area. However, surface area also decreases with increasing aggregation (Cismasu et al., 2011; Wang et al., 2016; Yin et al., 2011a; Yin et al., 2013). As previously observed (Lee et al., 2007; Yin et al., 2011a) and discussed above, Zn-coprecipitation caused greater aggregation and decreased crystallinity. The net effect of these two competing factors likely accounted for the overall trend of SSA in acid birnessite. For δ-$MnO_2$, increasing Zn/Mn ratio caused a continuous decrease of the SSA from 221.9 (p-dMn) to 131.6 $m^2/g$ (20Zn-dMn), suggesting aggregation to be the dominant factor affecting SSA in the δ-$MnO_2$ system.

Zn-coprecipitation also affected the surface charge of Mn oxides (Figure S2), a critical factor controlling the sorption and redox reactions of metals, metalloids, and organics with Mn oxides (Patil et al., 2007; Power et al., 2005; Villalobos et al., 2014b). Mn oxides synthesized in this study had negative zeta potential values even at pH as low as 2–3. Zn-coprecipitation caused these values to become less negative, likely at least partially due to the formation of $Zn^{2+}$ inner-sphere complexes on the oxide surfaces because $Zn^{2+}$ has strong tendency to sorb on $MnO_x$ and low compatibility for structural incorporation into $MnO_x$. Similar effects on surface charge were also previously observed during $Zn^{2+}$ adsorption onto birnessite (Power et al., 2005).

### 3.4. X-ray diffraction

XRD analysis was conducted to characterize the long-range order of all acid birnessite and δ-$MnO_2$ samples (Figure 2). The XRD patterns of pure acid birnessite and δ-$MnO_2$ both agreed well with previous studies (Chen et al., 2002; Drits et al., 1997; Lanson et al., 2000; Zhu et al., 2012) and showed no presence of any additional phases. For all acid birnessite and δ-$MnO_2$ phases (pure and Zn-coprecipitated), the d-spacing ratio of the peaks at 2.41 Å (11, 20) and 1.41 Å (31,

02) was 1.71, close to $\sqrt{3}$, indicating a hexagonal layer symmetry (Drits et al., 2007; Drits et al., 1997). Full width at half maximum (FWHM) of the (001) peaks for all acid birnessite samples was measured and the crystallite size along *c* axis was calculated using the Scherrer equation (Table 1). All δ-$MnO_2$ phases showed no obvious peak at ~7.23 Å (001) and only a broad peak at ~3.68 Å (002), due to the weaker layer stacking of δ-$MnO_2$ along *c* axis compared to acid birnessite phases. This is consistent with previous studies (Grangeon et al., 2012; Villalobos et al., 2006) and our HRTEM observations. Overall, Zn-coprecipitation had more impacts on vertical layer stacking for birnessite phases, while δ-$MnO_2$ phases are more affected in lateral layer size, as detailed below.

For birnessite phases, Zn-coprecipitation caused significant reduction in layer stacking. With increasing $Zn^{2+}$ content, XRD showed decreased peak height and increased peak width at 7.23 Å (00l) and/or 3.62 (002) reflections, suggesting decreased crystallinity and less layer stacking along the *c* axis, consistent with HRTEM observations. The vertical crystallite size calculated using Scherrer's equation also showed decreasing values with increasing $Zn^{2+}$ contents (Table 1). Such effect on layer stacking was a result from the coprecipitation process, as Zn sorption (during mineral formation) on the vacancy sites disrupted layer formation. In contrast, when $Zn^{2+}$ was equilibrated with hexagonal birnessite (orderly stacked) and exchanged for $H^+$, the 3D periodicity along *c* axis was preserved, although with a different stacking symmetry (monoclinic) (Lanson et al., 2002b). Reduced layer stacking was also observed before in Ni, Co, Fe and P coprecipitated birnessite samples (Wang et al., 2016; Yin et al., 2011a; Yin et al., 2013; Yin et al., 2012). As shown in the zoomed view (Figure 2C), the hump at 1.6–1.9 Å were previously suggested to reflect heavy metal adsorption on vacancy sites (Drits et al., 2007; Grangeon et al., 2008; Villalobos et al., 2006). With increasing $Zn^{2+}$ content, this hump became more significant due to vacancy site occupation by $Zn^{2+}$ (Drits et al., 2007; Grangeon et al., 2008).

For δ-$MnO_2$ phases, the presence of $Zn^{2+}$ did not cause significant changes in layer stacking, likely due to the already low numbers of layer stacking as shown in HRTEM and the weak intensity of XRD peaks at 7.23 and 3.62 Å (Figure 2B). At lower d-spacing range (Figure 2D), significantly decrease in peak intensities and increase in peak width were observed with increasing $Zn^{2+}$ content, suggesting decreased lateral coherent scattering domain (CSD) size (Wang et al., 2016) caused by the presence of $Zn^{2+}$, which was also observed in Fe (Yin et al., 2013) and P doped MnOx (Wang et al., 2016). This phenomenon is not obvious in our Zn coprecipitated acid birnessite samples.

### 3.5. X-ray absorption spectroscopy

#### *Mn K-edge XANES spectroscopy*

Linear combination fitting (LCF) of Mn K-edge XANES spectra was applied to determine the average oxidation state (AOS) and relative contribution of Mn(II), Mn(III), and Mn(IV) species in each sample (Figure 3, Fitting 1 using reference set 1). In several studies, δ-$MnO_2$ is common standard with an AOS close to 4.0 (Jürgensen et al., 2004; Villalobos et al., 2006; Villalobos et al., 2003). Lower values were also reported (3.84 in Webb et al (Webb et al., 2005a), 3.76 in Grangeon et al (Grangeon et al., 2012), 3.74 in Grangeon et al (Grangeon et al., 2008)) indicating the presence of mixed valence of Mn, i.e., adsorbed Mn(II,III) at vacancy sites and Mn(III) within layers. In this study, pure δ-$MnO_2$ has an AOS of 3.77 and ~15% Mn(III) contents, both are similar to the values in Grangeon et al (Grangeon et al., 2012). Compared to δ-$MnO_2$, pure acid birnessite has a higher AOS (3.92), which is very close to previously reported values, 3.9–4.0 (Toner et al., 2006; Villalobos et al., 2006; Villalobos et al., 2003; Wang et al., 2012a). Less Mn(II,III) contents was observed in acid birnessite compared to δ-$MnO_2$. For δ-$MnO_2$ samples, increasing $Zn^{2+}$ content resulted in the significant decrease of Mn(II) and Mn(III), increase of Mn(IV), thus an overall

increase of AOS. The replacement of interlayer Mn(II, III) by exotic cations was also observed during Zn, Pb and Cd adsorption on synthetic phyllomanganates (Grangeon et al., 2012; Lanson et al., 2002b). The AOS of acid birnessite showed no significant change with increasing $Zn^{2+}$, likely due to the already low Mn(II, III) contents in pure acid birnessite thus the replacement effects were not significant.

A second fitting of the Mn XANES data (Fitting 2) was conducted using reference set $MnSO_4$(s), $Mn_2O_3$, and pyrolusite ($MnO_2$) (Figure S5). The AOS of pure acid birnessite (3.79) and δ-$MnO_2$ (3.71) from Fitting 2 are lower than Fitting 1, confirming that LCF fitting method to achieve Mn AOS largely depends on the reference compounds. Based on the results of Fitting 2, Mn AOS of acid birnessite had no significant change with increasing Zn content, as compared to an increase of AOS for δ-$MnO_2$ samples, similar to the trend obtained from Fitting 1.

***Mn K-edge EXAFS spectroscopy***

Mn EXAFS spectroscopy was used to elucidate the local coordination environments (e.g. layer structure) of the oxide samples. $K^3$-weighted EXAFS spectra of pure and Zn-coprecipitated oxides and corresponding Fourier transforms (FT) are shown in Figure 4. For Mn EXAFS spectra, the region at ~8–9.2 $Å^{-1}$ (vertical dashed lines in Figure 4A and C) is sensitive to the layer symmetry of Mn oxides (Gaillot et al., 2007; Gaillot et al., 2003; Marcus et al., 2004). The amplitude of the two peaks at ~8.1 and 9.2 Å decreased while Mn oxides aged from hexagonal to triclinic (Learman et al., 2011b; Tang et al., 2014; Zhao et al., 2016). Peak broadening (and even splitting) is due to Mn(III) enrichment and ordering in triclinic birnessite (Manceau et al., 2004; Manceau et al., 2005; Marcus et al., 2004). Zhu et al. also used the sharpness of the two peaks to estimate the layer Mn(III) contents in biogenic Mn oxides (Zhu et al., 2010). Pure δ-$MnO_2$ has

hexagonal symmetry with low Mn(III) content and ordering, and showed sharp peaks in this region (Figure 4C) (Zhu et al., 2010). Pure acid birnessite (Figure 4A) showed even sharper peaks compared to pure δ-$MnO_2$, suggesting the least amount of layer Mn(III) among all samples, which is consistent with the highest AOS measured by Mn XANES analysis (Figure 3). With increasing $Zn^{2+}$ content, the peak at 9.2 $Å^{-1}$ of δ-$MnO_2$ samples became sharper, suggesting a decrease of layer Mn(III) content and ordering. For Zn-birnessite samples, no obvious changes were observed in this region, and all samples showed sharp peaks indicating low Mn(III) content and ordering.

FT spectra of all samples showed two dominant peaks at ~1.5 and 2.5 Å, corresponding to the Mn-O and Mn-Mn edge-sharing (Mn-$Mn_{edge}$) shells, respectively (Manceau and Combes, 1988). Previous studies suggested the peak height ratio $H_{Mn\text{-}Mn(edge)}/H_{Mn\text{-}o}$ corresponds to several factors such as layer vacancy site occupation fraction($f_{occ}$) and particle size (Saratovsky et al., 2006; Zhu et al., 2010). Saratovsky et al. found the ratios in layered Mn oxides increase with a larger layer cation occupation fraction(Saratovsky et al., 2006). However, several studies found different results from the trend above when it comes to vacancy occupation by Mn(III) incorporation into layer structure. For example, triclinic birnessite has large amounts of layer Mn(III) occupying vacancy sites (Lanson et al., 2002a) and a low ratio of 0.73 (Figure 4D). This ratio was 0.82 in pure δ-$MnO_2$ and 1.01 in pure acid birnessite, both of which have less layer Mn(III) and more unoccupied vacancies compared to triclinic birnessite (Tebo et al., 2004; Zhao et al., 2016). The aging process of abiotic (Zhao et al., 2016) and biogenic (Learman et al., 2011b; Tang et al., 2014) Mn oxides with Mn(II) results in more vacancy occupation by Mn(III) and decreased $H_{Mn\text{-}Mn}/H_{Mn\text{-}o}$ ratio. Zhu et al found the inverse proportionality between $f_{occ}$ and $H_{Mn\text{-}Mn}/H_{Mn\text{-}o}$ ratio and used this relationship to estimate layer Mn(III) contents in biogenic Mn oxides (Zhu et al., 2010). The decreased ratio probably attributes to Jahn-Teller distortions caused by layer Mn(III) which splits

the Mn-Mn peak and decreased the amplitude (Drits et al., 1997; Gaillot et al., 2003; Lanson et al., 2002b; Marcus et al., 2004; Webb et al., 2005b).

For δ-$MnO_2$ with Zn addition, decreased particle size could reduce the relative amplitude of Mn-$Mn_{edge}$ peak (Kawashima et al., 1986; Wang et al., 2016; Webb et al., 2005a) while less layer Mn(III) in Zn δ-$MnO_2$ samples could increase the amplitude (Sherman and Peacock, 2010; Webb et al., 2005a; Zhu et al., 2010). In this study, $H_{Mn\text{-}Mn(edge)}/H_{Mn\text{-}o}$ increased slightly from 0.82 (pure) to 0.91 (20Zn-dMn). This indicates the dominating factor is layer Mn(III) decreased by Zn addition as shown both in the k space (Figure 4C) and EXAFS fitting results below. The ratio remained relatively stable with increasing $Zn^{2+}$ content for the acid birnessite system showing relatively stable layer Mn(III) contents. This is also consistent with the unchanged peak sharpness at ~8–9.2 $Å^{-1}$ region in k space and our EXAFS fitting results of acid birnessite below.

Mn EXAFS fitting of all the oxide samples used a single scattering model considering the Mn-O, Mn-Mn edge sharing (Mn-$Mn_{edge}$), and Mn-Mn corner sharing (Mn-$Mn_{corner}$) paths (results in Table 2 and Figure 4). For pure and Zn-birnessite samples, best fits were obtained with ~6 O atoms at ~1.91–1.92 Å (consistent with Mn in octahedral coordination), ~5–6 Mn atoms at 2.87–2.88 Å, and ~1 Mn atom at 3.47–3.49 Å. The distances for the two Mn-Mn paths were consistent with previously reported values (Learman et al., 2011b; Manceau and Combes, 1988; Villalobos et al., 2006; Webb et al., 2005a). The Mn-$Mn_{edge}$ path is attributed to layer $MnO_6$ octahedra, and the coordination number (CN) can be affected by both particle size and layer vacancy site density (i.e. a fully filled $MnO_6$ layer has CN of 6; both decreasing particle size and increasing amount of vacancy sites will lead to smaller CN values). When Mn(III) incorporates in vacancy sites, increasing amount of layer Mn(III) would increase CN and result in a slightly longer Mn-$Mn_{edge}$ distance (Manceau et al., 2005; Villalobos et al., 2006; Zhu et al., 2010). The Mn-$Mn_{corner}$ path is

attributed to adsorbed interlayer Mn(II,III) ions (Villalobos et al., 2006; Zhu et al., 2010). Increasing amount of interlayer Mn(II) would result in a longer Mn-$Mn_{corner}$ distance, whereas increasing amount of interlayer Mn(III) would results in an increase in the CN (Webb et al., 2005a). For Zn-birnessite samples, increasing $Zn^{2+}$ content did not result in significant changes in the CNs and distances of these two Mn-Mn shells (except for the slight decrease of the Mn-$Mn_{corner}$ distance at 10 and 20% $Zn^{2+}$ contents), suggesting little changes to the vacancy site density and layer/interlayer Mn(III) contents. This is consistent with no changes in the 8–9.2 $Å^{-1}$ indicator region in the EXAFS spectra (Figure 4C), as well as the small changes in Mn(III) content and AOS as determined by the Mn XANES spectra. For δ-$MnO_2$, with increasing $Zn^{2+}$ content, the Mn-$Mn_{edge}$ path showed a decrease in distance from 2.884 (pure δ-$MnO_2$) to 2.871–2.872 Å (all the Zn-coprecipitated δ-$MnO_2$), suggesting less layer Mn(III) content. This was also observed in $Ni^{2+}$ coprecipitated biogenic Mn oxides (Zhu et al., 2010). The CN for the Mn-$Mn_{edge}$ path also decreased from 6.2 (pure δ-$MnO_2$) to 4.6–4.8 (Zn-coprecipitated δ-$MnO_2$). The decreased CN could result both from decrease in Mn(III) within layers and deduction of particle size. The Mn-$Mn_{corner}$ path showed decreased CN from 1.0 (pure δ-$MnO_2$) to 0.5 (20Zn-dMn), suggesting decreasing amount of adsorbed Mn(II,III) at interlayer region. A continuous decrease in distance was also observed for the Mn-$Mn_{corner}$ path, from 3.515 (pure δ-$MnO_2$) to 3.451 Å (20Zn-dMn), suggesting relatively less interlayer Mn(II) in the presence of $Zn^{2+}$ (Silvester et al., 1997).

### 3.6. Pair distribution function analysis

The PDF, G(r), for all pure and Zn-coprecipitated birnessite and δ-$MnO_2$ samples are shown in Figure 5. Compared to δ-$MnO_2$, acid birnessite has sharper peaks extending to longer R range, indicating better crystallinity and consistent with TEM and XRD results. The attenuation of

G(r) intensity can be used to estimate the size of coherent scattering domain (CSD) (Manceau et al., 2013; Nandy and Pradhan, 2015; Yin et al., 2015b; Zhu et al., 2012). Estimated CSD size is ~30 Å for δ-$MnO_2$ and ~50 Å for acid brinessite. Zn presence did not change the CSD size for both birnessite and δ-$MnO_2$ systems.

Figure 5(B, D) shows the G(r) in 1–7 Å range. PDF structural models for Mn oxides have been developed and discussed in previous studies (Manceau et al., 2013; Zhu et al., 2012) to describe the atomic pair contributions for the peaks in G(r). Based on these models, the first peak at ~1.9 Å is attributed to Mn-O atomic pairs within the $MnO_6$ layer. Based on Zn EXAFS analysis (Figure S3, Table S1), Zn exists as inner-sphere octahedrally coordinated surface complexes below/above vacancy sites for all Zn-coprecipitated birnessite and δ-$MnO_2$ samples, with the first shell Zn-O distance of 2.02–2.06 Å. For both birnessite and δ-$MnO_2$ system, no obvious changes were observed for this peak (Figure 5A&B), indicating little effects of Zn-O pairs on the peak at ~1.9 Å. The peak at ~2.85 Å corresponds to $(Mn\text{-}Mn)_{layer}$ and $(O\text{-}O)_{layer}$ pairs between two edge-sharing octahedra (Manceau et al., 2013; Zhu et al., 2012). With increasing Zn content, both birnessite and δ-$MnO_2$ showed decreased peak intensities and the decrease was more significant for the δ-$MnO_2$ system (Figure 5A and C). Increase of layer vacancy sites (i.e. less layer Mn) and/or reduced particle size can both cause such change. As discussed previously, the PDF CSD size for both the birnessite and δ-$MnO_2$ systems are not affected by Zn addition. Furthermore, Zn-Mn distance (due to Zn sorption) is at higher distance (above ~3.4 Å) for both the birnessite and δ-$MnO_2$ systems, therefore does not affect this peak. Therefore the change to this peak is more likely due to the increase of layer vacancy sites, consistent with Mn EXAFS fitting results. The peak at ~3.5 Å can be attributed to several atomic pairs: $(Mn\text{-}O)_{layer}$, $Mn_{layer}\text{-}Mn_{inter}$, $Mn_{inter}\text{-}O_{layer}$ (Zhu et al., 2012), as well as $Zn\text{-}Mn_1$ due to Zn sorption. For Zn-coprecipitated birnessite, this

peak intensity increased with increasing Zn content with no obvious changes in peak width and position. For Zn-coprecipitated δ-$MnO_2$, no obvious changes were observed for this peak. Due to the complexity of the contributing atomic pairs, these changes were not further analyzed.

## 4. Discussion

### 4.1. Layer stacking

Based on HRTEM observations, pure δ-$MnO_2$ had 5±1 layers and pure acid birnessite had 11±1 layers. Both numbers are higher than previously reported values obtained by XRD (3–4 layers for δ-$MnO_2$ and ~6 layers for acid birnessite) (Grangeon et al., 2012; Manceau et al., 2013; Villalobos et al., 2006). Other studies have also observed higher layer numbers from TEM than XRD (Grangeon et al., 2012), likely because XRD is sensitive to coherent scattering domains (i.e., bending and fault-stacked particles are less accounted for) (Manceau et al., 2013). In this study, all the oxide samples showed significant bending and stacking faults of the $MnO_6$ layers (and more significant with $Zn^{2+}$ impact); therefore, we used HRTEM to estimate the numbers of stacked layers.

Both birnessite and δ-$MnO_2$ showed decreases in layer stacking with increasing $Zn^{2+}$ content. Disturbed layer stacking has also been previously observed during Ni, Co, Fe, and V coprecipitation with acid birnessite and $Zn^{2+}$ coprecipitation with biogenic Mn oxides (Liu et al., 2015; Yin et al., 2011a; Yin et al., 2015b; Yin et al., 2014; Yin et al., 2013; Yin et al., 2012), and were attributed to the replacement of interlayer alkaline cations ($Na^+$, $K^+$) by foreign metals (Yu et al., 2013). With increasing $Zn^{2+}$ content, we observed significant disruption of layer stacking for birnessite as compared to the small changes in layer stacking for δ-$MnO_2$ (HRTEM and XRD). Meanwhile, significant decrease of $K^+$ content was also observed for acid birnessite (Table 1),

while no obvious changes were observed for the overall alkaline cation content ($K^+$ and $Na^+$) for δ-$MnO_2$.

### 4.2. Interlayer structure

Zn EXAFS spectra (Figure S3) and fitting results (Table S1) revealed that $Zn^{2+}$ formed inner-sphere complexes ($Zn^{IV}$ or $Zn^{VI}$) above/below the vacancy sites, consistent with the coordination environments during its adsorption onto biogenic and synthetic birnessite phases as well as coprecipitation with biogenic Mn oxides (Manceau et al., 2002; Silvester et al., 1997; Toner et al., 2006; Yu et al., 2013). No previous studies have observed $Zn^{2+}$ substitution at vacancy sites, likely due to the large size difference between octahedrally coordinated $Zn^{2+}$ (ionic radius 0.60 Å) and Mn(III) (more likely to exist as low-spin state (Yin et al., 2012), 0.58Å) or Mn(IV) (0.53 Å) (Shannon, 1976), as well as the large crystal field stabilization energy required for $Zn^{2+}$ to enter vacancy sites (Kwon et al., 2013). As discussed above, the interlayer alkali cation content was much higher for acid birnessite (~2.7 mmol $g^{-1}$ in pure birnessite) than δ-$MnO_2$ (~1.1 mmol $g^{-1}$ in pure δ-$MnO_2$), and showed more obvious decrease with increasing $Zn^{2+}$ contents (Table 1), suggesting more $Zn^{2+}$ replacement. Compared to alkali cations, the release of Mn(II)/Mn(III) by surface adsorbed $Zn^{2+}$ was more significant in the δ-$MnO_2$ system. This was confirmed by the consistent decrease in Mn(II)/Mn(III) contents and increase in AOS from XANES fitting (Figure 3), as well as the decrease of Mn-$Mn_{corner}$ CN in Mn EXAFS fitting (Table 2). The slight decrease in the Mn-$Mn_{corner}$ path distance suggests that the ratio of Mn(II)/Mn(III) is lower in Zn-coprecipitated δ-$MnO_2$ samples. This indicates that Mn(II) is less strongly bound to layers and the expelling effects of Mn(II) is more significant compared to Mn(III).

### 4.3. Layer structure

Based on previous studies and the results above, $Zn^{2+}$ repelling of layer Mn(III) is more likely to happen in phyllomanganate phases with low AOS and high Mn(III). Grangeon et al. found that $Zn^{2+}$ expelled Mn(III) during its adsorption on δ-$MnO_2$ with an AOS of 3.76 with ~13% layer Mn(III) (Grangeon et al., 2012). Similar effects were also observed in our Zn-coprecipitated δ-$MnO_2$ systems with an AOS of 3.77 and ~15% Mn(III) contents. However, our EXAFS fitting results showed no change of the Mn-$Mn_{edge}$ CN and distance for the acid birnessite system, suggesting that $Zn^{2+}$ addition did not significantly affect layer Mn(III) contents in acid birnessite phases. This is possibly due to the already low content of layer Mn(III) in acid birnessite (AOS 3.92, ~6% Mn(III)), causing the Mn(III) expelling effect by $Zn^{2+}$ to be not as obvious as the δ-$MnO_2$ system. Natural biogenic Mn oxides are typically nanocrystalline phases with lower AOS and more Mn(III) contents than synthetic phyllomanganate analogs (i.e., acid birnessite and δ-$MnO_2$) (Toner et al., 2006; Villalobos et al., 2006; Villalobos et al., 2003; Webb et al., 2005a; Zhu et al., 2010), therefore, one might expect that $Zn^{2+}$ can cause significant modifications of biogenic MnOx layer structure. Boonfueng et al. on $Zn^{2+}$ presence during biogenic $MnO_x$ formation showed modifications to the 8–9.2 $Å^{-1}$ EXAFS indicator region, although the authors concluded no structural changes (Boonfueng et al., 2009).

The reduction of layer size can be attributed to pH change and/or crystal growth inhibition caused by $Zn^{2+}$ addition. First, metal doping during phyllomanganate synthesis is a common method for producing $MnO_x$ materials with desired properties, though the pH change caused by metal hydrolysis were rarely measured or discussed in previous studies (Yin et al., 2015a; Yin et al., 2015b; Yin et al., 2011b; Yin et al., 2015c; Yin et al., 2012). In this study, the addition of $Zn^{2+}$ slightly decreased the pH in the synthesis solutions (Figure S7). Yu et al. also found that $Zn^{2+}$

addition decreased the pH of fungi growing media during the formation of biogenic $MnO_x$ (Yu et al., 2013). Grangeon et al. found that acidic condition caused the dissolution and smaller layer size when pre-formed δ-$MnO_2$ was equilibrated at low pH (Grangeon et al., 2014). Secondly, previous studies have indicated that addition of foreign oxyanions (phosphate, silicate and sulfate) can inhibit the layer growth of acid birnessite. These oxyanions should not significantly change the pH of the synthesis environment but still reduced the layer size by inhibiting crystal growth (Wang et al., 2016; Yin et al., 2015b). The effects of Zn co-precipitation with biogenic Mn oxides in a well-buffered media in ongoing to investigate the significance of these two factors.

### 4.4. Particle size

Particle size can significantly change the electrochemical (Gao et al., 2001; Li et al., 2016; Wang et al., 2016), catalytic (Wang et al., 2016), adsorptive, and redox properties of phyllomanganates (Villalobos et al., 2014a; Villalobos et al., 2014b). BET Surface area (Villalobos et al., 2014b; Villalobos et al., 2006; Webb et al., 2005a), TEM (Grangeon et al., 2012; Villalobos et al., 2003), XRD (Grangeon et al., 2012; Zhang et al., 2011) and PDF (Hammersley et al., 1996; Yin et al., 2015b; Zhu et al., 2012) have been used to estimate the size dimensions of Mn oxides. Size estimation of phyllomanganates using BET surface area is difficult due to the complex morphology and strong aggregation, and can be simplified using a spherical model (Villalobos et al., 2014b). Smaller particle size in Zn-coprecipitated samples, as revealed by other techniques, was supposed to expose more external surfaces, yet less surface area was observed by BET due to aggregation (Yin et al., 2011a). Therefore, much caution should be taken when BET specific surface area is utilized to estimate the size of heavily aggregated particles.

Estimation of acid birnessite and δ-$MnO_2$ particle size by TEM images is difficult due to

strong aggregation. Lateral particle sizes (along the *a*-*b* plane) of ~50–200 nm for acid birnessite and ~20–100 nm for δ-$MnO_2$, can be concluded based on a previous study (Villalobos et al., 2003) and our HRTEM observation. With increasing $Zn^{2+}$ content, our HRTEM analysis observed a general decrease of layer stacking and lateral particle size. Curling and faults of the $MnO_6$ nanosheets can lead to less periodicity in the *a*-*b* plane and less layer stacking consistency along *c* axis (Grangeon et al., 2012; Post and Veblen, 1990; Zhu et al., 2012). Along with texture effects (Manceau et al., 2013), this might be the reason that the CSD size calculated by XRD and PDF are much smaller than the particle size observed by HRTEM. Indeed, the CSD size revealed by PDF is around 5 nm for acid birnessite and 2–3 nm for δ-$MnO_2$ (Figure 5). The XRD calculated birnessite CSD size along *c* axis is 4–7 nm, agreed quite well with the PDF results, but both smaller than HRTEM measured size.

Interestingly, with increasing $Zn^{2+}$ content, the PDF CSD size barely changed for both acid birnessite and δ-$MnO_2$ (Figure 5), while broaden peaks in XRD (Figure 2) indicated decreasing CSD size along *c* axis (especially acid birnessite) and in *a*-*b* plane (especially δ-$MnO_2$) (Wang et al., 2016). Foreign $Zn^{2+}$ caused more incoherence in both phyllomanganates, e.g. layer collapse, curling, stacking faults and large amorphous aggregated area, which significantly broadened XRD Bragg peaks and decreased crystallite sizes. However, for PDF which detects both Bragg and diffuse scatterings, decreased crystallinity and formation of sub-domains, although decreasing the peak sharpness, would not affect the longest atomic pair distances which determined the signal fall-offs and CSD size.

## 5. Conclusions

This systematic study demonstrated that the impact of $Zn^{2+}$ during phyllomanganate (acid

birnessite and δ-$MnO_2$) formation are much more significant than by $Zn^{2+}$ adsorption alone (Grangeon et al., 2012). $Zn^{2+}$ neutralized the negative surface charge of phyllomanganates and caused great particle aggregation. The introduced $Zn^{2+}$ during acid birnessite formation expelled interlayer alkaline cations and water molecules and interrupted the layer stacking along *c* axis. The AOS of δ-$MnO_2$ increased due to Mn(II)/Mn(III) expelling by $Zn^{2+}$, while such effect was not obvious in the acid birnessite system due to the already high AOS and little Mn(II, III) in acid birnessite. $Zn^{2+}$ existed as inner-sphere surface complexes ($Zn^{IV}$ or $Zn^{VI}$) above/below vacancy sites as adsorbed species instead of substitution at vacancy sites. $Zn^{2+}$ decreased Mn(III) contents within $MnO_x$ layers, leaving more vacancy sites available for future reactions (e.g. sorption of other cations). For acid birnessite, layer stacking and interlayer cations/water molecules are significantly affected with minimal modulation of the layer structure. The modification of layer structure (e.g. crystallinity and layer Mn(III) contents) is much more significant in the δ-$MnO_2$ system.

Previous studies have shown that birnessite structure interruption caused by foreign metals is in the reverse relationship with the compatibility (Co > Ni >Fe) of metals in birnessite layers (Yin et al., 2013). This study provides insights on the possible prediction of structural changes caused by $Zn^{2+}$ and other similar incompatible cations on natural and synthetic phyllomanganates with different crystallinity. The sorptive ability of these metal impacted oxides are expected to change significantly due to the less negative surface charge, decreased particle size, and increased vacancy site density (Villalobos et al., 2014a; Villalobos et al., 2014b; Wang et al., 2012b; Yin et al., 2011a; Yin et al., 2012; Zhao et al., 2010). $Zn^{2+}$ also decreased Mn(II, III) contents and increased AOS in the oxides with high Mn(II, III) contents, which, together with the modified sorptive reactivity, can potentially have great influences on the oxidative reactivity, transformation,

and microbial anaerobic respiration of Mn oxides (Nico and Zasoski, 2000; Tebo et al., 2004; Villalobos et al., 2014a; Villalobos et al., 2014b). These factors can also potentially change the band gap and other catalytic properties of Mn oxides (Kang et al., 2017; Lee et al., 2007; Lucht and Mendoza-Cortes, 2015).

**Acknowledgements**

S. Zhao and Y. Tang acknowledge funding support from U.S. National Science Foundation (NSF) under grant No. 1710285 and the National Aeronautics and Space Administration (NASA) under grant No. NNA15BB03A. Q. Wang and M. Zhu acknowledge funding support from NSF under Grant No. EAR-1529937. We thank Dr. Hailong Chen (Georgia Tech) for help with XRD analysis. We also appreciate the support from beamline scientists Drs. Benjamin Reinhart and Sungsik Lee (APS Beamline 12BM), Qing Ma (APS Beamline 5-BM-D), and Ryan Davis (SSRL Beamline 4-1) on experiment setup. Portions of this research were conducted at the Advanced Photon Source (APS) and Stanford Synchrotron Radiation Lightsource (SSRL). APS is a U.S. Department of Energy (DOE) Office of Science User Facility operated for the DOE Office of Science by Argonne National Laboratory under Contract No. DE-AC02-06CH11357. Use of SSRL, SLAC National Accelerator Laboratory, is supported by DOE Office of Science, Office of Basic Energy Sciences under Contract No. DE-AC02-76SF00515.

**Supporting Information**

Details of BET surface area, zeta potential, HRTEM, XRD, Zn XAS, and PDF analysis; Zn EXAFS shell-by-shell fitting results; stacking layer observations by HTREM; HRTEM images; zeta potential data; Zn EXAFS shell-by-shell fitting results; PDF data; Mn XANES spectra and LCF results; change of solution pH during $MnO_x$ synthesis.

**Table 1.** Sample label, chemical composition, BET surface area, HRTEM revealed numbers of stacking layer per particle, as well as XRD determined crystallite size along *c* axis for the Zn-coprecipitated birnessite and δ-$MnO_2$ samples.

| Initial Zn/Mn molar ratio | Sample label | Chemical composition of the final solids | | | | | BET specific surface area ($m^2/g$) | Number of stacking layers (by HRTEM) | Crystallite size along *c* axis (nm, by XRD) |
|---|---|---|---|---|---|---|---|---|---|
| | | Mn (wt%) | Zn (wt%) | K (wt%) | Na (wt%) | Zn/Mn molar ratio | | | |
| ***Acid birnessite*** | | | | | | | | | |
| 0 | p-bir | 45.2 | 0 | 10.5 | - | 0 | 27.4±0.4 | 11±3 | 6.4 |
| 1% | 1Zn-bir | 44.9 | 0.6 | 9.5 | - | 1.1% | 30.2±0.5 | 11±3 | 6.7 |
| 5% | 5Zn-bir | 45.9 | 2.9 | 8.1 | - | 5.7% | 32.5±0.3 | 9±4 | 5.6 |
| 10% | 10Zn-bir | 43.8 | 6.0 | 4.9 | - | 12.4% | 29.2±0.2 | 7±2 | 5.1 |
| 20% | 20Zn-bir | 43.3 | 8.0 | 1.4 | - | 15.9% | 19.3±0.2 | 5±1 | 4.5 |
| ***δ-$MnO_2$*** | | | | | | | | | |
| 0 | p-dMn | 37.2 | 0 | 1.0 | 2.0 | 0 | 221.9±1.3 | 5±1 | - |
| 1% | 1Zn-dMn | 37.4 | 1.3 | 1.7 | 1.7 | 2.2% | 159.2±1.0 | 5±1 | - |
| 5% | 5Zn-dMn | 38.3 | 2.4 | 2.1 | 1.8 | 4.2% | 123.9±0.7 | 5±1 | - |
| 20% | 20Zn-dMn | 37.3 | 9.8 | 2.1 | 1.2 | 21.2% | 131.6±1.0 | 4±1 | - |

**Table 2.** Mn EXAFS fitting results for pure and Zn-coprecipitated acid birnessite and δ-$MnO_2$ samples.

| Sample label | R | Shell | CN | Distance(Å) | $\sigma^2$ |
|---|---|---|---|---|---|
| ***Acid birnessite*** | | | | | |
| p-bir | 0.0049 | Mn-O | 6.0 (0.8) | 1.919 (0.006) | 0.007 (0.001) |
| | | $Mn\text{-}Mn_{edge}$ | 5.5 (0.8) | 2.877 (0.007) | 0.007 (0.001) |
| | | $Mn\text{-}Mn_{corner}$ | 0.9 (0.7) | 3.487 (0.047) | 0.007 (0.001) |
| 1Zn-bir | 0.0094 | Mn-O | 6.0 (1.1) | 1.916 (0.009) | 0.006 (0.002) |
| | | $Mn\text{-}Mn_{edge}$ | 5.8 (1.2) | 2.877 (0.009) | 0.007 (0.001) |
| | | $Mn\text{-}Mn_{corner}$ | 1.0 (1.0) | 3.491 (0.058) | 0.007 (0.001) |
| 5Zn-bir | 0.0032 | Mn-O | 6.3 (0.7) | 1.914 (0.005) | 0.007 (0.001) |
| | | $Mn\text{-}Mn_{edge}$ | 5.5 (0.7) | 2.871 (0.005) | 0.007 (0.001) |
| | | $Mn\text{-}Mn_{corner}$ | 0.9 (0.6) | 3.490 (0.033) | 0.007 (0.001) |
| 10Zn-bir | 0.0183 | Mn-O | 7.0 (1.5) | 1.913 (0.013) | 0.008 (0.002) |
| | | $Mn\text{-}Mn_{edge}$ | 5.2 (1.3) | 2.869 (0.013) | 0.006 (0.002) |
| | | $Mn\text{-}Mn_{corner}$ | 0.9 (1.1) | 3.476 (0.083) | 0.006 (0.002) |
| 20Zn-bir | 0.0081 | Mn-O | 6.7 (1.1) | 1.914 (0.008) | 0.007 (0.001) |
| | | $Mn\text{-}Mn_{edge}$ | 5.2 (1.0) | 2.868 (0.009) | 0.006 (0.001) |
| | | $Mn\text{-}Mn_{corner}$ | 1.0 (0.8) | 3.469 (0.045) | 0.006 (0.001) |
| ***δ-$MnO_2$*** | | | | | |
| p-dMn | 0.0077 | Mn-O | 5.6 (0.9) | 1.921 (0.008) | 0.005 (0.001) |
| | | $Mn\text{-}Mn_{edge}$ | 6.2 (0.9) | 2.884 (0.008) | 0.008 (0.001) |
| | | $Mn\text{-}Mn_{corner}$ | 1.0 (0.8) | 3.515 (0.061) | 0.008 (0.001) |
| 1Zn-dMn | 0.0049 | Mn-O | 6.0 (0.8) | 1.914 (0.006) | 0.005 (0.001) |
| | | $Mn\text{-}Mn_{edge}$ | 4.9 (1.0) | 2.872 (0.007) | 0.008 (0.001) |
| | | $Mn\text{-}Mn_{corner}$ | 0.8 (0.9) | 3.453 (0.054) | 0.008 (0.001) |
| 5Zn-dMn | 0.0034 | Mn-O | 6.8 (0.6) | 1.913 (0.005) | 0.006 (0.001) |
| | | $Mn\text{-}Mn_{edge}$ | 4.8 (0.6) | 2.871 (0.005) | 0.006 (0.001) |
| | | $Mn\text{-}Mn_{corner}$ | 0.6 (0.5) | 3.471 (0.040) | 0.006 (0.001) |
| 20Zn-dMn | 0.0075 | Mn-O | 6.9 (1.0) | 1.910 (0.007) | 0.006 (0.001) |
| | | $Mn\text{-}Mn_{edge}$ | 4.7 (1.1) | 2.871 (0.009) | 0.007 (0.001) |
| | | $Mn\text{-}Mn_{corner}$ | 0.5 (0.8) | 3.451 (0.049) | 0.007 (0.001) |

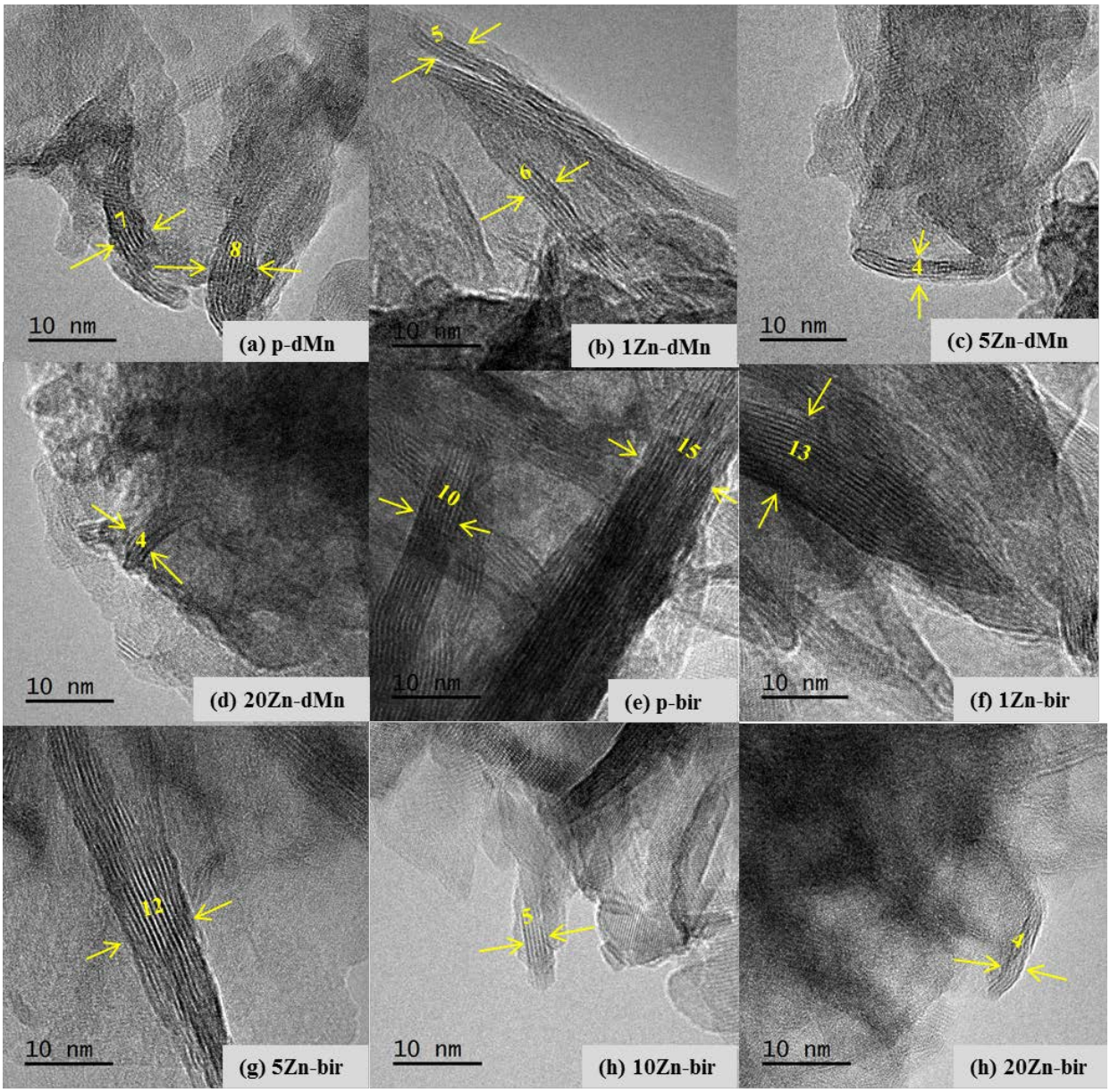


**Figure 1.** HRTEM images of pure and Zn-coprecipitated δ-$MnO_2$ and birnessite samples. (a) p-dMn (b) 1Zn-dMn, (c) 5Zn-dMn and (d) 20Zn-dMn for δ-$MnO_2$; (e) p-bir (f) 1Zn-bir, (g) 5Zn-bir, (h) 10Zn-bir and (i) 20Zn-bir for acid birnessite. Yellow numbers indicate the number of stacking layers between the yellow arrows.

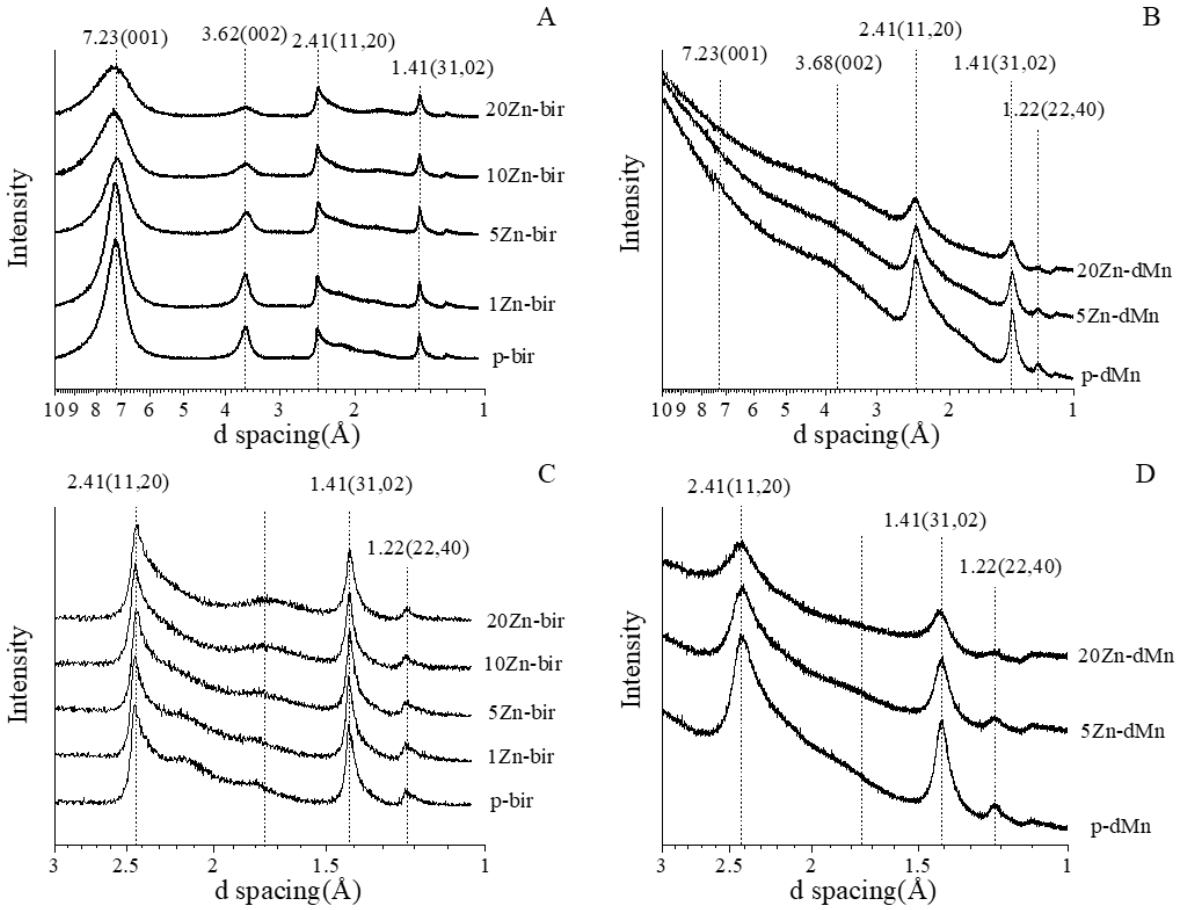


**Figure 2.** XRD patterns of pure and Zn-coprecipitated birnessite (A) and δ-$MnO_2$ (B), as well as their zoomed view at 1–3 Å (C and D, respectively).

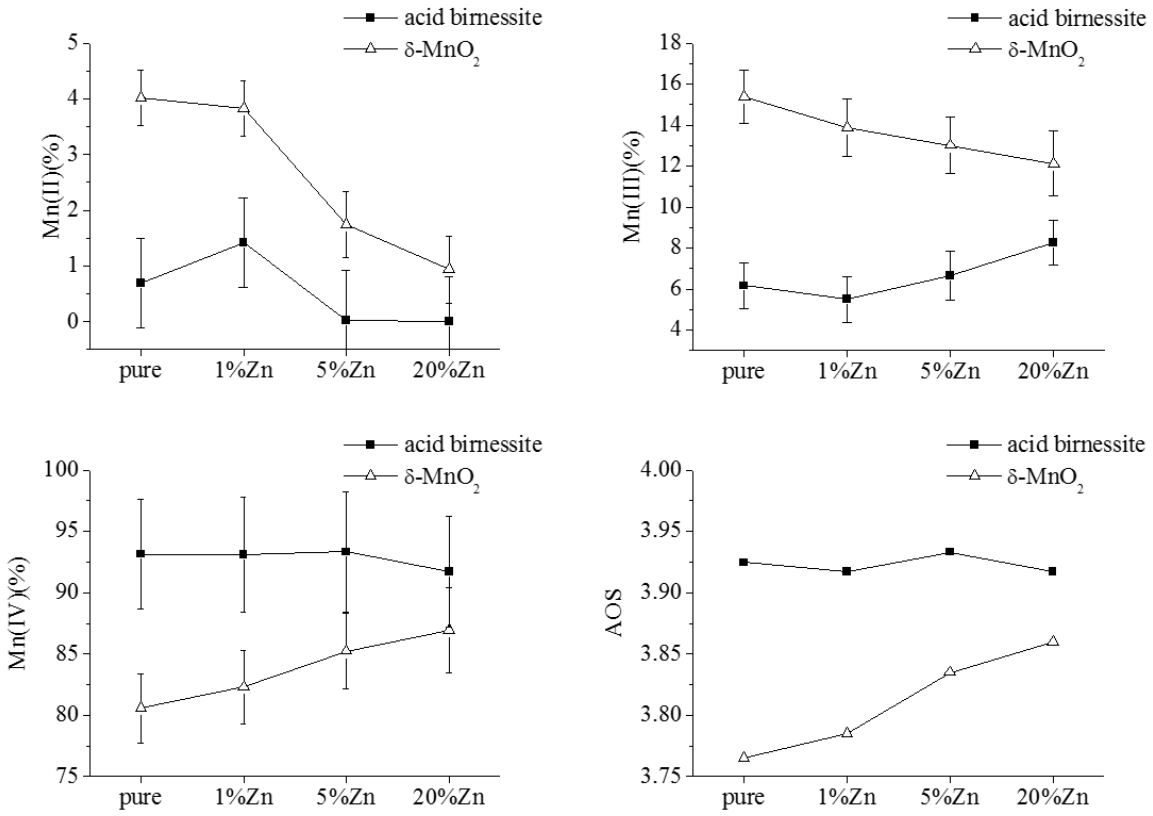


**Figure 3.** Relative percentage of Mn(II), (III), and (IV), as well as average oxidation states (AOS) of pure and Zn-coprecipitated birnessite and δ-$MnO_2$ phases as determined by linear combination fitting of Mn K-edge XANES using reference set 1.

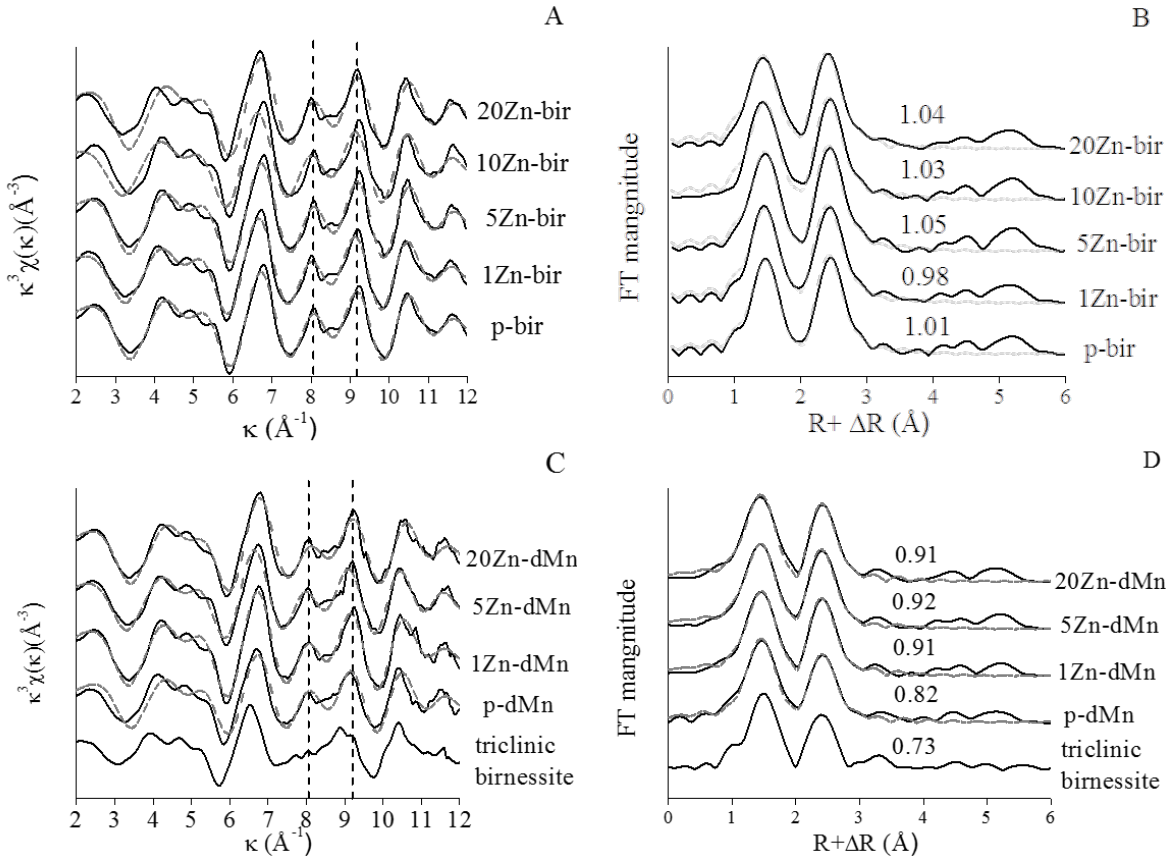


**Figure 4**. $k^3$-weighted Mn K-edge EXAFS and Fourier transformed (FT) spectra (not corrected for phase shift) of pure and Zn-coprecipitated acid birnessite (A, B) and δ-$MnO_2$ (C, D). Raw and fitted data are in solid and dotted lines, respectively. Triclinic birnessite was also plotted to compare with δ-$MnO_2$ samples. Vertical dashed lines in (A) and (C) highlight the indicator region. The ratios of second shell (Mn-Mn edge sharing) and first shell (Mn-O) in FT spectra are shown in (B) and (D).

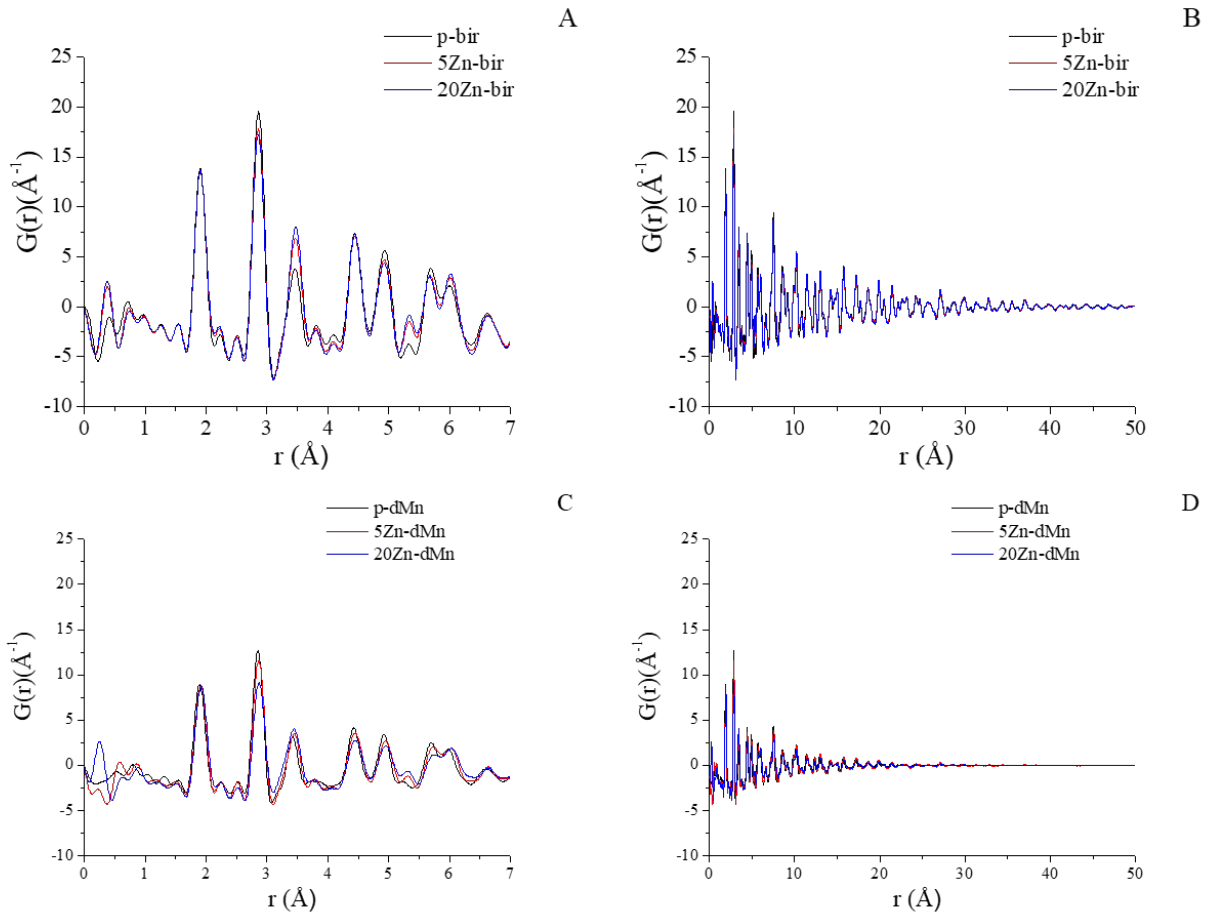


**Figure 5.** PDF of pure and Zn-coprecipitated Mn oxides plotted at 7 (left) and 50 Å scales (right). (A, B) acid birnessite, (C, D) δ-$MnO_2$.

## References


Bargar, J.R., Fuller, C.C., Marcus, M.A., Brearley, A.J., De la Rosa, M.P., Webb, S.M., Caldwell, W.A., 2009. Structural characterization of terrestrial microbial Mn oxides from Pinal Creek, AZ. Geochimica et Cosmochimica Acta, 73(4): 889-910.

Bargar, J.R., Tebo, B.M., Bergmann, U., Webb, S.M., Glatzel, P., Chiu, V.Q., Villalobos, M., 2005. Biotic and abiotic products of Mn (II) oxidation by spores of the marine Bacillus sp. strain SG-1. American Mineralogist, 90(1): 143-154.

Bodeï, S., Manceau, A., Geoffroy, N., Baronnet, A., Buatier, M., 2007. Formation of todorokite from vernadite in Ni-rich hemipelagic sediments. Geochimica et Cosmochimica Acta, 71(23): 5698-5716.

Boonfueng, T., Axe, L., Yee, N., Hahn, D., Ndiba, P.K., 2009. Zn sorption mechanisms onto sheathed *Leptothrix discophora* and the impact of the nanoparticulate biogenic Mn oxide coating. Journal of Colloid and Interface Science, 333(2): 439-447.

Chang, Y.-Y., Lim, J.-W., Yang, J.-K., 2012. Removal of As(V) and Cr(VI) in aqueous solution by sand media simultaneously coated with Fe and Mn oxides. Journal of Industrial and Engineering Chemistry, 18(1): 188-192.

Charlet, L., Manceau, A.A., 1992. X-ray absorption spectroscopic study of the sorption of Cr (III) at the oxide-water interface: II. Adsorption, coprecipitation, and surface precipitation on hydrous ferric oxide. Journal of colloid and interface science, 148(2): 443-458.

Chen, X., Shen, Y.-F., Suib, S.L., O'Young, C., 2002. Characterization of manganese oxide octahedral molecular sieve (M-OMS-2) materials with different metal cation dopants. Chemistry of Materials, 14(2): 940-948.

111 Childs, C.W., 1975. Composition of iron-manganese concretions from some New Zealand soils.
112 Geoderma, 13(2): 141-152.
113 Cismasu, A.C., Michel, F.M., Tcaciuc, A.P., Tyliszczak, T., Brown Jr, G.E., 2011. Composition
114 and structural aspects of naturally occurring ferrihydrite. Comptes Rendus Geoscience,
115 343(2): 210-218.
116 Drits, V.A., Lanson, B., Bougerol-Chaillout, C., Gorshkov, A.I., Manceau, A., 2002. Structure of
117 heavy-metal sorbed birnessite: Part 2. Results from electron diffraction. American
118 Mineralogist, 87(11-12): 1646-1661.
119 Drits, V.A., Lanson, B., Gaillot, A.-C., 2007. Birnessite polytype systematics and identification by
120 powder X-ray diffraction. American Mineralogist, 92(5-6): 771-788.
121 Drits, V.A., Silvester, E., Gorshkov, A.I., Manceau, A., 1997. Structure of synthetic monoclinic
122 Na-rich birnessite and hexagonal birnessite: I. Results from X-ray diffraction and selected-
123 area electron diffraction. American Mineralogist, 82(9-10): 946-961.
124 Gadde, R.R., Laitinen, H.A., 1974. Heavy metal adsorption by hydrous iron and manganese oxides.
125 Analytical Chemistry, 46(13): 2022-2026.
126 Gaillot, A.-C., Drits, V.A., Manceau, A., Lanson, B., 2007. Structure of the synthetic K-rich
127 phyllomanganate birnessite obtained by high-temperature decomposition of $KMnO_4$:
128 Substructures of K-rich birnessite from 1000 °C experiment. Microporous and Mesoporous
129 Materials, 98(1-3): 267-282.
130 Gaillot, A.C., Flot, D., Drits, V.A., Manceau, A., Burghammer, M., Lanson, B., 2003. Structure of
131 synthetic K-rich birnessite obtained by high-temperature decomposition of $KMnO_4$. I.
132 Two-layer polytype from 800 degrees C experiment. Chemistry of Materials, 15(24): 4666-
133 4678.

134 Gao, Q., Giraldo, O., Tong, W., Suib, S.L., 2001. Preparation of Nanometer-Sized Manganese
135 Oxides by Intercalation of Organic Ammonium Ions in Synthetic Birnessite OL-1.
136 Chemistry of Materials, 13(3): 778-786.
137 Grangeon, S., Lanson, B., Lanson, M., 2014. Solid-state transformation of nanocrystalline
138 phyllomanganate into tectomanganate: influence of initial layer and interlayer structure.
139 Acta Crystallographica Section B: Structural Science, Crystal Engineering and Materials,
140 70(5): 828-838.
141 Grangeon, S., Lanson, B., Lanson, M., Manceau, A., 2008. Crystal structure of Ni-sorbed synthetic
142 vernadite: a powder X-ray diffraction study. Mineralogical Magazine, 72(6): 1279-1291.
143 Grangeon, S., Lanson, B., Miyata, N., Tani, Y., Manceau, A., 2010. Structure of nanocrystalline
144 phyllomanganates produced by freshwater fungi. American Mineralogist, 95(11-12): 1608-
145 1616.
146 Grangeon, S., Manceau, A., Guilhermet, J., Gaillot, A.-C., Lanson, M., Lanson, B., 2012. Zn
147 sorption modifies dynamically the layer and interlayer structure of vernadite. Geochimica
148 et Cosmochimica Acta, 85: 302-313.
149 Hammersley, A., 1998. FIT2D V9. 129 Reference Manual V3. 1. Inter Rep ESRF98HA01, ESRF,
150 Grenoble.
151 Hammersley, A., Svensson, S., Hanfland, M., Fitch, A., Hausermann, D., 1996. Two-dimensional
152 detector software: from real detector to idealised image or two-theta scan. International
153 Journal of High Pressure Research, 14(4-6): 235-248.
154 Hinkle, M.A., Dye, K.G., Catalano, J.G., 2017. Impact of Mn(II)-Manganese Oxide Reactions on
155 Ni and Zn Speciation. Environmental Science & Technology, 51: 3187-3196.

Jenkyns, H.C., 1970. Fossil manganese nodules from the west Sicilian Jurassic. Eclogae Geologicae Helvetiae, 63(3): 741-774.

Jürgensen, A., Widmeyer, J.R., Gordon, R.A., Bendell-Young, L.I., Moore, M.M., Crozier, E.D., 2004. The structure of the manganese oxide on the sheath of the bacterium Leptothrix discophora: An XAFS study. American Mineralogist, 89(7): 1110-1118.

Kamimura, A., Nozaki, Y., Nishiyama, M., Nakayama, M., 2013. Oxidation of benzyl alcohols by semi-stoichiometric amounts of cobalt-doped birnessite-type layered $MnO_2$ under oxygen atmosphere. RSC Advances, 3(2): 468-472.

Kang, Q., Vernisse, L., Remsing, R.C., Thenuwara, A.C., Shumlas, S.L., McKendry, I.G., Klein, M.L., Borguet, E., Zdilla, M.J., Strongin, D.R., 2017. Effect of Interlayer Spacing on the Activity of Layered Manganese Oxide Bilayer Catalysts for the Oxygen Evolution Reaction. Journal of the American Chemical Society: 1863-1870.

Kawashima, M., Tainaka, Y., Hori, T., Koyama, M., Takamatsu, T., 1986. Phosphate adsorption onto hydrous manganese(IV) oxide in the presence of divalent cations. Water Research, 20(4): 471-475.

Kung, K., McBride, M., 1988. Electron transfer processes between hydroquinone and hausmannite ($Mn_3O_4$). Clays and Clay Minerals, 36: 297-302.

Kwon, K.D., Refson, K., Sposito, G., 2009. Zinc surface complexes on birnessite: A density functional theory study. Geochimica et Cosmochimica Acta, 73(5): 1273-1284.

Kwon, K.D., Refson, K., Sposito, G., 2013. Understanding the trends in transition metal sorption by vacancy sites in birnessite. Geochimica et Cosmochimica Acta, 101: 222-232.

Lanson, B., Drits, V.A., Feng, Q., Manceau, A., 2002a. Structure of synthetic Na-birnessite: Evidence for a triclinic one-layer unit cell. American Mineralogist, 87(11-12): 1662-1671.

Lanson, B., Drits, V.A., Gaillot, A.-C., Silvester, E., Plançon, A., Manceau, A., 2002b. Structure of heavy-metal sorbed birnessite: Part 1. Results from X-ray diffraction. American Mineralogist, 87(11-12): 1631-1645.

Lanson, B., Drits, V.A., Silvester, E., Manceau, A., 2000. Structure of H-exchanged hexagonal birnessite and its mechanism of formation from Na-rich monoclinic buserite at low pH. American Mineralogist, 85(5-6): 826-838.

Lanson, B., Marcus, M.A., Fakra, S., Panfili, F., Geoffroy, N., Manceau, A., 2008. Formation of Zn–Ca phyllomanganate nanoparticles in grass roots. Geochimica et Cosmochimica Acta, 72(10): 2478-2490.

Learman, D., Voelker, B., Vazquez-Rodriguez, A., Hansel, C., 2011a. Formation of manganese oxides by bacterially generated superoxide. Nature Geoscience, 4(2): 95-98.

Learman, D.R., Wankel, S.D., Webb, S.M., Martinez, N., Madden, A.S., Hansel, C.M., 2011b. Coupled biotic–abiotic Mn(II) oxidation pathway mediates the formation and structural evolution of biogenic Mn oxides. Geochimica et Cosmochimica Acta, 75(20): 6048-6063.

Lee, S.H., Kim, T.W., Park, D.H., Choy, J.-H., Hwang, S.-J., Jiang, N., Park, S.-E., Lee, Y.-H., 2007. Single-step synthesis, characterization, and application of nanostructured $K_xMn_{1-y}Co_yO_{2-\delta}$ with controllable chemical compositions and crystal structures. Chemistry of Materials, 19(20): 5010-5017.

Li, H., Liu, F., Zhu, M., Feng, X., Zhang, J., Yin, H., 2015. Structure and properties of Co-doped cryptomelane and its enhanced removal of $Pb^{2+}$ and $Cr^{3+}$ from wastewater. Journal of Environmental Sciences, 34: 77-85.

Li, W.N., Yuan, J., Shen, X.F., Gomez‐Mower, S., Xu, L.P., Sithambaram, S., Aindow, M., Suib, S.L., 2006. Hydrothermal synthesis of structure‐ and shape‐controlled manganese

oxide octahedral molecular sieve nanomaterials. Advanced Functional Materials, 16(9): 1247-1253.

Li, Y.R., Marschilok, A.C., Takeuchi, E.S., Takeuchi, K.J., 2016. Synthesis of copper birnessite, $Cu_xMnO_y \cdot nH_2O$ with crystallite size control: Impact of crystallite size on electrochemistry. Journal of the Electrochemical Society, 163(2): A281-A285.

Liu, L., Min, M., Liu, F., Yin, H., Zhang, Y., Qiu, G., 2015. Influence of vanadium doping on the supercapacitance performance of hexagonal birnessite. Journal of Power Sources, 277: 26-35.

Lucht, K.P., Mendoza-Cortes, J.L., 2015. Birnessite: A layered manganese oxide to capture sunlight for water-splitting catalysis. Journal of Physical Chemistry C, 119(40): 22838-22846.

Manceau, A., Combes, J., 1988. Structure of Mn and Fe oxides and oxyhydroxides: a topological approach by EXAFS. Physics and Chemistry of Minerals, 15(3): 283-295.

Manceau, A., Lanson, B., Drits, V.A., 2002. Structure of heavy metal sorbed birnessite. Part III: Results from powder and polarized extended X-ray absorption fine structure spectroscopy. Geochimica et Cosmochimica Acta, 66(15): 2639-2663.

Manceau, A., Lanson, M., Geoffroy, N., 2007. Natural speciation of Ni, Zn, Ba, and As in ferromanganese coatings on quartz using X-ray fluorescence, absorption, and diffraction. Geochimica et Cosmochimica Acta, 71(1): 95-128.

Manceau, A., Marcus, M.A., Grangeon, S., 2012. Determination of Mn valence states in mixed-valent manganates by XANES spectroscopy. American Mineralogist, 97(5-6): 816-827.

Manceau, A., Marcus, M.A., Grangeon, S., Lanson, M., Lanson, B., Gaillot, A.-C., Skanthakumar, S., Soderholm, L., 2013. Short-range and long-range order of phyllomanganate

nanoparticles determined using high-energy X-ray scattering. Journal of Applied Crystallography, 46(1): 193-209.

Manceau, A., Marcus, M.A., Tamura, N., Proux, O., Geoffroy, N., Lanson, B., 2004. Natural speciation of Zn at the micrometer scale in a clayey soil using X-ray fluorescence, absorption, and diffraction. Geochimica et Cosmochimica Acta, 68(11): 2467-2483.

Manceau, A., Silvester, E., Bartoli, C., Lanson, B., Drits, V.A., 1997. Structural mechanism of $Co^{2+}$ oxidation by the phyllomanganate buserite. American Mineralogist, 82(11-12): 1150-1175.

Manceau, A., Tamura, N., Celestre, R.S., MacDowell, A.A., Geoffroy, N., Sposito, G., Padmore, H.A., 2003. Molecular-scale speciation of Zn and Ni in soil ferromanganese nodules from loess soils of the Mississippi Basin. Environmental Science & Technology, 37(1): 75-80.

Manceau, A., Tommaseo, C., Rihs, S., Geoffroy, N., Chateigner, D., Schlegel, M., Tisserand, D., Marcus, M.A., Tamura, N., Chen, Z.-S., 2005. Natural speciation of Mn, Ni, and Zn at the micrometer scale in a clayey paddy soil using X-ray fluorescence, absorption, and diffraction. Geochimica et Cosmochimica Acta, 69(16): 4007-4034.

Marcus, M.A., Manceau, A., Kersten, M., 2004. Mn, Fe, Zn and As speciation in a fast-growing ferromanganese marine nodule. Geochimica Et Cosmochimica Acta, 68(14): 3125-3136.

Nandy, A., Pradhan, S., 2015. Effects of monovalent cation doping on the structure, microstructure, lattice distortion and magnetic behavior of single crystalline NdMnO3 compounds. Dalton Transactions, 44(39): 17229-17240.

Nico, P.S., Zasoski, R.J., 2000. Importance of Mn(III) availability on the rate of Cr(III) oxidation on δ-$MnO_2$. Environmental Science & Technology, 34(16): 3363-3367.

247 Patil, S., Sandberg, A., Heckert, E., Self, W., Seal, S., 2007. Protein adsorption and cellular uptake
248 of cerium oxide nanoparticles as a function of zeta potential. Biomaterials, 28(31): 4600-
249 4607.
250 Peña, J., Bargar, J.R., Sposito, G., 2015. Copper sorption by the edge surfaces of synthetic
251 birnessite nanoparticles. Chemical Geology, 396: 196-207.
252 Peña, J., Kwon, K.D., Refson, K., Bargar, J.R., Sposito, G., 2010. Mechanisms of nickel sorption
253 by a bacteriogenic birnessite. Geochimica et Cosmochimica Acta, 74(11): 3076-3089.
254 Poizot, P., Laruelle, S., Grugeon, S., Dupont, L., Tarascon, J., 2000. Nano-sized transition-metal
255 oxides as negative-electrode materials for lithium-ion batteries. Nature, 407(6803): 496-
256 499.
257 Post, J.E., Veblen, D.R., 1990. Crystal structure determinations of synthetic sodium, magnesium,
258 and potassium birnessite using TEM and the Rietveld method. American Mineralogist,
259 75(5-6): 477-489.
260 Power, L.E., Arai, Y., Sparks, D.L., 2005. Zinc adsorption effects on arsenite oxidation kinetics at
261 the birnessite-water interface. Environmental Science & Technology, 39(1): 181-187.
262 Qiu, X., Thompson, J.W., Billinge, S.J., 2004. PDFgetX2: a GUI-driven program to obtain the pair
263 distribution function from X-ray powder diffraction data. Journal of Applied
264 Crystallography, 37(4): 678-678.
265 Ravel, B., Newville, M., 2005. ATHENA, ARTEMIS, HEPHAESTUS: Data analysis for X-ray
266 absorption spectroscopy using IFEFFIT. Journal of Synchrotron Radiation, 12: 537-541.
267 Ressler, T., 1998. WinXAS: a program for X-ray absorption spectroscopy data analysis under MS-
268 Windows. Journal of Synchrotron Radiation, 5(2): 118-122.

Saratovsky, I., Gurr, S.J., Hayward, M.A., 2009. The structure of manganese oxide formed by the fungus Acremonium sp. strain KR21-2. Geochimica et Cosmochimica Acta, 73(11): 3291-3300.

Saratovsky, I., Wightman, P.G., Pastén, P.A., Gaillard, J.-F., Poeppelmeier, K.R., 2006. Manganese oxides: parallels between abiotic and biotic structures. Journal of the American Chemical Society, 128(34): 11188-11198.

Shannon, R., 1976. Revised effective ionic radii and systematic studies of interatomic distances in halides and chalcogenides. Acta Crystallographica Section A: Crystal Physics, Diffraction, Theoretical and General Crystallography, 32(5): 751-767.

Sherman, D.M., Peacock, C.L., 2010. Surface complexation of Cu on birnessite ($\delta$-$MnO_2$): controls on Cu in the deep ocean. Geochimica et Cosmochimica Acta, 74(23): 6721-6730.

Silvester, E., Manceau, A., Drits, V.A., 1997. Structure of synthetic monoclinic Na-rich birnessite and hexagonal birnessite: II. Results from chemical studies and EXAFS spectroscopy. American Mineralogist, 82(9-10): 962-978.

Simanova, A.A., Kwon, K.D., Bone, S.E., Bargar, J.R., Refson, K., Sposito, G., Peña, J., 2015. Probing the sorption reactivity of the edge surfaces in birnessite nanoparticles using nickel(II). Geochimica et Cosmochimica Acta.

Stone, A.T., Morgan, J.J., 1984. Reduction and dissolution of manganese(III) and manganese(IV) oxides by organics. 1. Reaction with hydroquinone. Environmental Science & Technology, 18(6): 450-456.

Tan, H., Zhang, G., Heaney, P.J., Webb, S.M., Burgos, W.D., 2010. Characterization of manganese oxide precipitates from Appalachian coal mine drainage treatment systems. Applied Geochemistry, 25(3): 389-399.

292 Tang, Y., Webb, S.M., Estes, E.R., Hansel, C.M., 2014. Chromium(III) oxidation by biogenic
293 manganese oxides with varying structural ripening. Environmental Science: Processes &
294 Impacts, 16(9): 2127-2136.
295 Tebo, B.M., Bargar, J.R., Clement, B.G., Dick, G.J., Murray, K.J., Parker, D., Verity, R., Webb,
296 S.M., 2004. Biogenic manganese oxides: properties and mechanisms of formation. Annual
297 Review of Earth and Planetary Sciences, 32: 287-328.
298 Toner, B., Manceau, A., Webb, S.M., Sposito, G., 2006. Zinc sorption to biogenic hexagonal-
299 birnessite particles within a hydrated bacterial biofilm. Geochimica et Cosmochimica Acta,
300 70(1): 27-43.
301 Trivedi, P., Axe, L., Tyson, T.A., 2001. XAS Studies of Ni and Zn Sorbed to Hydrous Manganese
302 Oxide. Environmental Science & Technology, 35(22): 4515-4521.
303 Villalobos, M., Bargar, J., Sposito, G., 2005. Mechanisms of Pb(II) sorption on a biogenic
304 manganese oxide. Environmental Science & Technology, 39(2): 569-576.
305 Villalobos, M., Carrillo-Cárdenas, M., Gibson, R., López-Santiago, N.R., Morales, J.A., 2014a.
306 The influence of particle size and structure on the sorption and oxidation behaviour of
307 birnessite: II. Adsorption and oxidation of four polycyclic aromatic hydrocarbons.
308 Environmental Chemistry, 11(3): 279-288.
309 Villalobos, M., Escobar-Quiroz, I.N., Salazar-Camacho, C., 2014b. The influence of particle size
310 and structure on the sorption and oxidation behavior of birnessite: I. Adsorption of As(V)
311 and oxidation of As(III). Geochimica et Cosmochimica Acta, 125: 564-581.
312 Villalobos, M., Lanson, B., Manceau, A., Toner, B., Sposito, G., 2006. Structural model for the
313 biogenic Mn oxide produced by Pseudomonas putida. American Mineralogist, 91(4): 489-
314 502.

315 Villalobos, M., Toner, B., Bargar, J., Sposito, G., 2003. Characterization of the manganese oxide
316 produced by *Pseudomonas putida* strain MnB1. Geochimica et Cosmochimica Acta,
317 67(14): 2649-2662.
318 Wang, Q., Liao, X., Xu, W., Ren, Y., Livi, K.J., Zhu, M., 2016. Synthesis of birnessite in the
319 presence of phosphate, silicate, or sulfate. Inorganic Chemistry, 55(20): 10248-10258.
320 Wang, Y., Feng, X., Villalobos, M., Tan, W., Liu, F., 2012a. Sorption behavior of heavy metals
321 on birnessite: Relationship with its Mn average oxidation state and implications for types
322 of sorption sites. Chemical Geology, 292–293(0): 25-34.
323 Wang, Y., Feng, X., Villalobos, M., Tan, W., Liu, F., 2012b. Sorption behavior of heavy metals
324 on birnessite: Relationship with its Mn average oxidation state and implications for types
325 of sorption sites. Chemical Geology, 292–293: 25-34.
326 Webb, S., Tebo, B., Bargar, J., 2005a. Structural characterization of biogenic Mn oxides produced
327 in seawater by the marine Bacillus sp. strain SG-1. American Mineralogist, 90(8-9): 1342-
328 1357.
329 Webb, S.M., 2005. SIXpack: a graphical user interface for XAS analysis using IFEFFIT. Physica
330 Scripta, T115: 1011-1014.
331 Webb, S.M., Dick, G.J., Bargar, J.R., Tebo, B.M., 2005b. Evidence for the presence of Mn(III)
332 intermediates in the bacterial oxidation of Mn(II). Proceedings of the National Academy
333 of Sciences of the United States of America, 102(15): 5558-5563.
334 Yin, H., Dai, X., Zhu, M., Li, F., Feng, X., Liu, F., 2015a. Fe-doped cryptomelane synthesized by
335 refluxing at atmosphere: Structure, properties and photocatalytic degradation of phenol.
336 Journal of Hazardous materials, 296: 221-229.

Yin, H., Feng, X., Qiu, G., Tan, W., Liu, F., 2011a. Characterization of Co-doped birnessites and application for removal of lead and arsenite. Journal of Hazardous materials, 188(1): 341-349.

Yin, H., Feng, X., Tan, W., Koopal, L.K., Hu, T., Zhu, M., Liu, F., 2015b. Structure and properties of vanadium(V)-doped hexagonal turbostratic birnessite and its enhanced scavenging of $Pb^{2+}$ from solutions. Journal of Hazardous materials, 288: 80-88.

Yin, H., Li, H., Wang, Y., Ginder-Vogel, M., Qiu, G., Feng, X., Zheng, L., Liu, F., 2014. Effects of Co and Ni co-doping on the structure and reactivity of hexagonal birnessite. Chemical Geology, 381: 10-20.

Yin, H., Liu, F., Feng, X., Hu, T., Zheng, L., Qiu, G., Koopal, L.K., Tan, W., 2013. Effects of Fe doping on the structures and properties of hexagonal birnessites–Comparison with Co and Ni doping. Geochimica et Cosmochimica Acta, 117: 1-15.

Yin, H., Liu, F., Feng, X., Liu, M., Tan, W., Qiu, G., 2011b. $Co^{2+}$-exchange mechanism of birnessite and its application for the removal of $Pb^{2+}$ and As(III). Journal of Hazardous materials, 196: 318-326.

Yin, H., Liu, Y., Koopal, L.K., Feng, X., Chu, S., Zhu, M., Liu, F., 2015c. High Co-doping promotes the transition of birnessite layer symmetry from orthogonal to hexagonal. Chemical Geology, 410: 12-20.

Yin, H., Tan, W., Zheng, L., Cui, H., Qiu, G., Liu, F., Feng, X., 2012. Characterization of Ni-rich hexagonal birnessite and its geochemical effects on aqueous $Pb^{2+}$/$Zn^{2+}$ and As(III). Geochimica et Cosmochimica Acta, 93: 47-62.

Yu, Q., Sasaki, K., Tanaka, K., Ohnuki, T., Hirajima, T., 2013. Zinc sorption during bio-oxidation and precipitation of manganese modifies the layer stacking of biogenic birnessite. Geomicrobiology Journal, 30(9): 829-839.

Zhang, H., Bayne, M., Fernando, S., Legg, B., Zhu, M., Penn, R.L., Banfield, J.F., 2011. Size-dependent bandgap of nanogoethite. Journal of Physical Chemistry C, 115(36): 17704-17710.

Zhao, H., Zhu, M., Li, W., Elzinga, E.J., Villalobos, M., Liu, F., Zhang, J., Feng, X., Sparks, D.L., 2016. Redox reactions between Mn(II) and hexagonal birnessite change its layer symmetry. Environmental Science & Technology, 50(4): 1750-1758.

Zhao, W., Wang, Q.Q., Liu, F., Qiu, G.H., Tan, W.F., Feng, X.H., 2010. $Pb^{2+}$ adsorption on birnessite affected by $Zn^{2+}$ and $Mn^{2+}$ pretreatments. Journal of Soils and Sediments, 10(5): 870-878.

Zhu, M., Farrow, C.L., Post, J.E., Livi, K.J.T., Billinge, S.J.L., Ginder-Vogel, M., Sparks, D.L., 2012. Structural study of biotic and abiotic poorly-crystalline manganese oxides using atomic pair distribution function analysis. Geochimica et Cosmochimica Acta, 81: 39-55.

Zhu, M., Ginder-Vogel, M., Parikh, S.J., Feng, X.-H., Sparks, D.L., 2010. Cation effects on the layer structure of biogenic Mn-oxides. Environmental Science & Technology, 44(12): 4465-4471.